Symmetry rules shaping spin-orbital textures in surface states

Kenneth Gotlieb, Zhenglu Li, Chiu-Yun Lin, Chris Jozwiak, Ji Hoon Ryoo, Cheol-Hwan Park, Zahid Hussain, Steven G. Louie, and Alessandra Lanzara

Phys. Rev. B **95**, 245142 — Published 30 June 2017

DOI: 10.1103/PhysRevB.95.245142

Symmetry Rules Shaping Spin-Orbital Textures in Surface States

Kenneth Gotlieb,[1,2,*] Zhenglu Li,[2,3,*] Chiu-Yun Lin,[2,3] Chris Jozwiak,[4] Ji Hoon Ryoo,[5] Cheol-Hwan Park,[5] Zahid Hussain,[4] Steven G. Louie,[2,3,†] and Alessandra Lanzara[2,3,‡]

[1]*Graduate Group in Applied Science & Technology, University of California, Berkeley, California 94720, USA*

[2]*Materials Sciences Division, Lawrence Berkeley National Laboratory, Berkeley, California 94720, USA*

[3]*Department of Physics, University of California, Berkeley, California 94720, USA*

[4]*Advanced Light Source, Lawrence Berkeley National Laboratory, Berkeley, California 94720, USA*

[5]*Department of Physics and Center for Theoretical Physics, Seoul National University, Seoul 08826, Korea*

(Dated: March 13, 2017)

Abstract

Strong spin-orbit coupling creates exotic electronic states such as Rashba and topological surface states, which hold promise for technologies involving the manipulation of spin. Only recently has the complexity of these surface states been appreciated: they are composed of several atomic orbitals with distinct spin textures in momentum space. A complete picture of the wavefunction must account for this orbital dependence of spin. We discover that symmetry constrains the way orbital and spin components of a state co-evolve as a function of momentum, and from this, we determine the rules governing how the two degrees of freedom are interwoven. We directly observe this complexity in spin-resolved photoemission and *ab initio* calculations of the topological surface states of Sb(111), where the photoelectron spin direction near $\bar{\Gamma}$ is found to have a strong and unusual dependence on photon polarization. This dependence unexpectedly breaks down at large $|k|$, where the surface states mix with other nearby surface states. However, along mirror planes, symmetry protects the distinct spin orientations of different orbitals. Our discovery broadens the understanding of surface states with strong spin-orbit coupling, demonstrates the conditions that allow for optical manipulation of photoelectron spin, and will be highly instructive for future spintronics applications.

I. INTRODUCTION

Materials with strong spin-orbit coupling (SOC) and spin-split surface states have garnered significant attention for possible use in spintronic devices, in which the spin degree of freedom would be manipulated electrically[1–4]. While the proposed utility of Rashba or topological surface states stems from their spin textures in momentum space, these spin textures carry complexity not usually considered. The pseudospin described by commonly used models can actually correspond to several different momentum-dependent spin textures, each belonging to wavefunctions with distinct atomic orbital character.

In states subject to spin-orbit coupling, in the atomic limit, spin and orbital angular momenta ($\mathbf{S}$ and $\mathbf{L}$) are not good quantum numbers; total angular momentum $\mathbf{J}$ is instead the conserved quantity[5]. In fact, it has recently been observed in topological surface states that the spin and orbital textures can be "entangled" such that, at a given momentum, there is a mix of orbitals that each have a distinct spin orientation[5–8]. Thus, to fully understand the wavefunction of these potentially useful states means characterizing the complex spin-orbital texture.

While deepening our understanding of spin-orbit surface states, the dependence of spin texture on wavefunction atomic orbital character can give rise to a rich array of physical phenomena. It causes photoelectron spins to point in a direction dependent on photon polarization, allowing for optical control of spin polarization[9,10]. In fact, the relative weight of $p_{x,y,z}$ orbitals, and hence spin texture of Bi_2Se_3, varies through the atomic layers containing the surface state wavefunction[7,11]. Thus, many distinct spin polarization patterns are possible as different photoemission geometries will be sensitive to the interference of varying contributions from different layers[7]. It has even been seen that in Bi/Cu(111), hybridization at large momentum can abruptly change the relative strength of different orbital components and thereby change the overall spin polarization of a surface band[12]. That orbitals have distinct spin textures even enabled a photoemission experiment to reveal the strength of spin-orbit coupling in spin-degenerate bands in Sr_2RuO_4[13]. Knowledge of how the spin and orbital degrees of freedom mix is key to interpreting experimental results from spin-orbit materials, as well as possibly utilizing them technologically.

To reveal this spin-orbital texture, access is needed to specific orbitals' contributions to the spin-dependent electronic structure. Spin- and angle-resolved photoemission spectroscopy (spin-ARPES) with tunable photon polarization is uniquely capable of studying this, as demonstrated with the surface states of Bi_2Se_3, where the spin polarization of photoelectrons was observed to reverse for light polarization rotated 90°[7,10,11]. This effect was predicted based on symmetry arguments and a model Hamiltonian[9], and was further discussed microscopically in terms of the constituent atomic orbitals making up the band[5]. With total angular momentum as the conserved quantity, the $J_z = \pm\frac{1}{2}$ basis is used to describe the surface state near $\bar{\Gamma}$. Under this constraint, spin-orbit coupling gives each of the $p_{x,y,z}$ orbitals its own spin texture. Light will select p orbitals oriented along the direction of photon polarization according to the selection rules for the photoemission process[6].

This optically tunable spin texture was first studied in the topological surface state of Bi_2Se_3, in which the occupied surface state Dirac cone is near the Brillouin zone center and isotropic in momentum or $\mathbf{k}$ space. Previous discussion of this phenomenon therefore focused on strong spin-orbit coupling and the symmetries at the $\bar{\Gamma}$ point in Bi_2Se_3: time reversal, mirror, and C_3 rotational symmetry. Similar phenomena have been observed in Bi/Ag(111)[14], W(110)[15,16], and BiTeI[17]. Thus far, there have been no tests of how it evolves at high wavevector $\mathbf{k}$ as the symmetry changes, leaving open questions about the fundamental nature of coupling of orbital textures to distinct spin textures. While it is known that orbital components of a surface state can couple to distinct spins and that a band's overall spin texture can change as the relative strength of orbital components change, the rules that determine how a particular orbital couples to spin and how symmetry shapes this coupling across the Brillouin zone have never been clearly determined.

Antimony, a topologically non-trivial semimetal, provides an intriguing test case. The Sb(111) surface states have been investigated with ARPES and spin-ARPES, confirming the spin polarization due to strong SOC and nonzero Berry's phase[18–23]. While the (111) surface of Sb has the same symmetries as Bi_2Se_3, its surface states are distinct in their strong $\mathbf{k}$ dependence. They remain separate from the bulk states out to large $|k|$, allowing for a comparison of the spin-orbital texture near $\bar{\Gamma}$ to that in areas of reduced symmetry, where we will demonstrate that there are significant differences.

II. EXPERIMENTAL DETAILS

Single crystal Sb (Goodfellow Corp.) was cleaved in situ, exposing the (111) surface. It was kept at ≈80 K and inside ultrahigh vacuum of $\approx 5 \times 10^{-11}$ Torr. The sample was probed with 6 eV photons generated through fourth harmonic generation from a Ti:sapphire oscillator and examined with a high efficiency spin- and angle-resolved photoemission spectrometer. Instrumental energy resolution was 15 meV and momentum resolution was ± 0.02 Å^{-1}. The instrument and its use with a laboratory laser have been described previously[24,25].

The spectrometer detects electron energy by the time-of-flight down a drift tube, allowing measurement of an entire energy distribution curve (EDC) at once. The light arrives 45° from the direction of detected photoelectrons. As shown in Fig. 4a, the angle of the sample with respect to the analyzer (labeled θ) is rotated to scan emission angle, which corresponds to cutting along k_x. The spin-TOF system achieves very efficient spin detection with a low energy exchange scattering polarimeter.

The rapid data collection allows exploration of a wide experimental phase space, including measuring spin-ARPES spectra with different probing photon polarizations. Measurements were made with both s-polarized (linear vertical, $\hat{\epsilon}$ entirely in the sample plane) and p-polarized photons (linear horizontal, $\hat{\epsilon}$ includes an out-of-plane component). In this work, the spin polarization, defined as $P = (I_\uparrow - I_\downarrow)/(I_\uparrow + I_\downarrow)$ where I is photoemission intensity, was always measured along $\hat{y}$, the component of spin that is allowed by symmetry along mirror planes. It is worth noting, however, that when experiments are performed with light that is polarized at an angle between s- and p-polarized, finite P_x and P_z spin polarizations are allowed and can yield information about the interference between $+P_y$ and $-P_y$ components of the wavefunction[26].

III. SPIN-RESOLVED ARPES RESULTS

A spin-integrated ARPES map along $\bar{\Gamma}$-$\bar{K}$ and $\bar{\Gamma}$-$\bar{M}$ high-symmetry directions is shown in Fig. 1a alongside a schematic (Fig. 1b) of the bands indicating the spin texture measured previously,[19,20] that of the dominant p_z orbitals. This work will show that this is part of a larger, more complex spin texture. We will use this finding to demonstrate rules governing the coupling of spins to orbitals. Along $\bar{\Gamma}$-$\bar{M}$, two surface bands cross the Fermi level near $\bar{\Gamma}$. However, along $\bar{\Gamma}$-$\bar{K}$, the lower one bends back down towards the bulk valence band rather than cross E_F. Spin-resolved EDCs measured with p-polarized light at two momenta (Fig. 1c,d) corroborate this picture. The lower band appears red for $k_x < 0$, indicating

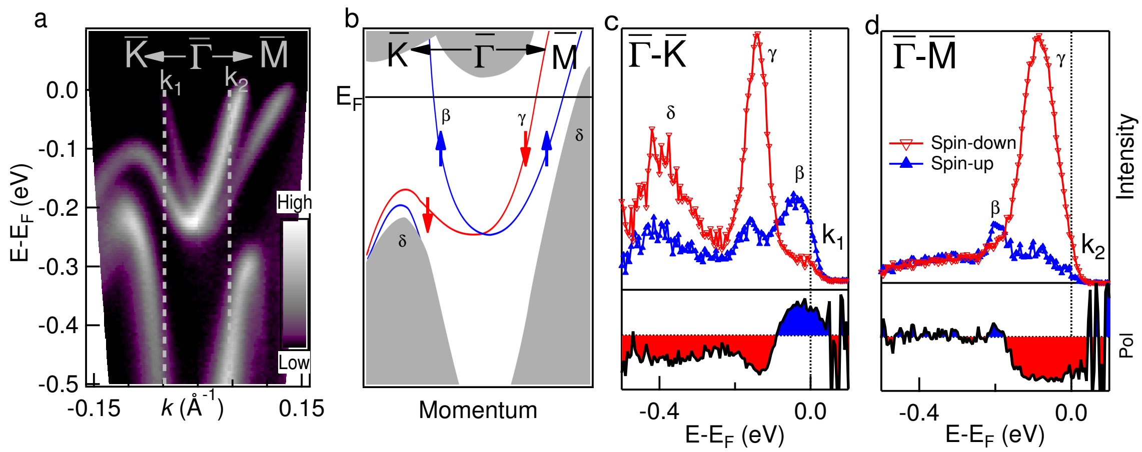

FIG. 1. **The surface states of Sb(111), as measured with p-polarized (linear horizontal) light. a,** Spin-integrated ARPES map along $\bar{\Gamma}$-$\bar{\mathrm{K}}$ ($-k_x$) and $\bar{\Gamma}$-$\bar{\mathrm{M}}$ ($+k_x$) directions. **b,** Schematic of the surface states, color-coded to indicate spin polarizations measured previously[20]. Blue indicates $P_y > 0$, as defined in 3 a,d, and red indicates $P_y < 0$. **c,d,** Representative spin-resolved energy distribution curves (EDCs) taken at momenta shown in a. The spin-polarization, defined as $P_y = (I_\uparrow - I_\downarrow)/(I_\uparrow + I_\downarrow)$, is shown below corresponding EDCs.

$P_y < 0$, while the upper band is blue, indicating $P_y > 0$ on that side of the Brillouin zone.

Figure 2 shows spin-resolved EDCs at select momenta along cuts through both high symmetry directions. By following the maximum peak positions (marked as β, γ, δ,), the spin characters of the bulk valence band and the two surface bands are resolved. Panels b and e show stacks of spin-resolved EDCs along $\bar{\Gamma}$-$\bar{\mathrm{M}}$ and $\bar{\Gamma}$-$\bar{\mathrm{K}}$, respectively. The corresponding spin polarizations for the two high symmetry directions are shown in panels c and f. The intensity peak is primarily spin-up (blue) for the surface band β while it is primarily spin-down (red) for the surface band γ. At the outer Fermi level crossings along $\bar{\Gamma}$-$\bar{\mathrm{M}}$, the absolute value of the spin polarization for both surface state bands is greater than 60% (-67% for γ in k_1 and +65% for β in k_6). As the $\bar{\Gamma}$ point is approached along $\bar{\Gamma}$-$\bar{\mathrm{M}}$, the spin polarization decreases to -47% for γ in k_3 and +34% for β in k_4. Intriguingly, the bulk valence band (δ) shows a small spin polarization of +12% in k_1.

Surprisingly, when the experiment is performed with s-polarized photons, as shown in Figure 3, we observe an overall reversal of the spin polarization near the $\bar{\Gamma}$ point. The β band now shows a negative spin polarization while γ shows a positive polarization. Along $\bar{\Gamma}$-$\bar{\mathrm{M}}$, γ now has a polarization of +25% at k_1: somewhat weaker in magnitude than what was measured with p-polarized light, perahps due to imperfect light polarization. We believe that, as was the case for Bi_2Se_3[10], this spin reversal is a manifestation of strong spin-orbital entanglement. Specifically, p_x, p_y, and p_z orbitals couple to different spin textures and are each probed by different polarization components of light. Interestingly, we observe that far from the $\bar{\Gamma}$ point along $\bar{\Gamma}$-$\bar{\mathrm{K}}$, the spin polarization does not reverse upon rotation of light. This is seen in comparing spectra at k_1, k_2, k_5, and k_6 along $\bar{\Gamma}$-$\bar{\mathrm{K}}$ betwen Fig. 2 and 3.

Figure 4 shows the full spin-resolved energy maps for both spin-up and spin-down electrons along $\bar{\Gamma}$-$\bar{\mathrm{M}}$ and $\bar{\Gamma}$-$\bar{\mathrm{K}}$ for both light polarizations. The maps are obtained by combining thirty EDCs and are shown with a colorscale in which brightness (from light to dark) corresponds to total photoemission intensity while color (from red to blue) corresponds to spin polarization. These two-dimensional colorscales are scaled nonlinearly in order to clearly resolve each band.

Beginning with the $\bar{\Gamma}$-$\bar{\mathrm{M}}$ direction, the data taken with p-polarized light (Fig. 4a) match the cartoon of Fig. 1b and previous measurements[19,20]. The $\bar{\Gamma}$ point is enclosed within an electron pocket with positive spin polarization for $-k_x$ and negative spin polarization for $+k_x$. The two branches of the surface state meet at $\bar{\Gamma}$ and bend back up to the Fermi level. Note that with p-polarized light, the stronger photoemission matrix elements for the spin-down branch (also apparent in 1c,d and 2), which can be strongly affected by experimental

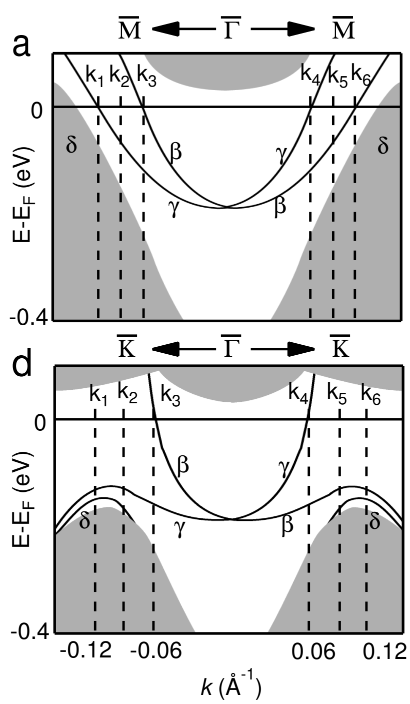

FIG. 2. **Spin-Resolved measurements with p-polarized light a,** Schematic of bandstructure along $\bar{\Gamma}$-$\bar{\mathrm{M}}$ with positions of measurements marked by dashed lines. **b,** Spin-resolved EDCs at momenta marked in a. Peaks are marked corresponding to bands in a. **c,** Spin-polarization corresponding to EDCs in b. **d-f** Same as a-c but along the $\bar{\Gamma}$-$\bar{\mathrm{K}}$ direction.

geometry[27], yield a net negative measured spin polarization at the $\bar{\Gamma}$ point.

However, when the same map is made with s-polarized light (Fig. 4b), both surface bands show the opposite spin polarization. The upper electron pocket encloses $\bar{\Gamma}$ with spin-down electrons at $-k_x$ and spin-up at $+k_x$. The lower branches also fully reverse their spins at all momenta from $\bar{\Gamma}$ to $k_x \approx \pm 0.13\text{Å}^{-1}$, when they cross E_F. Furthermore, as in Bi_2Se_3, the spin polarization can be adjusted continuously, as shown in Fig. 4c, by rotating the angle of linear photon polarization, effectively selecting the orientation of p orbitals being photoemitted.

The $\bar{\Gamma}$-$\bar{\mathrm{K}}$ direction (Fig. 4d-f) demonstrates a strong contrast. The same spin dependence

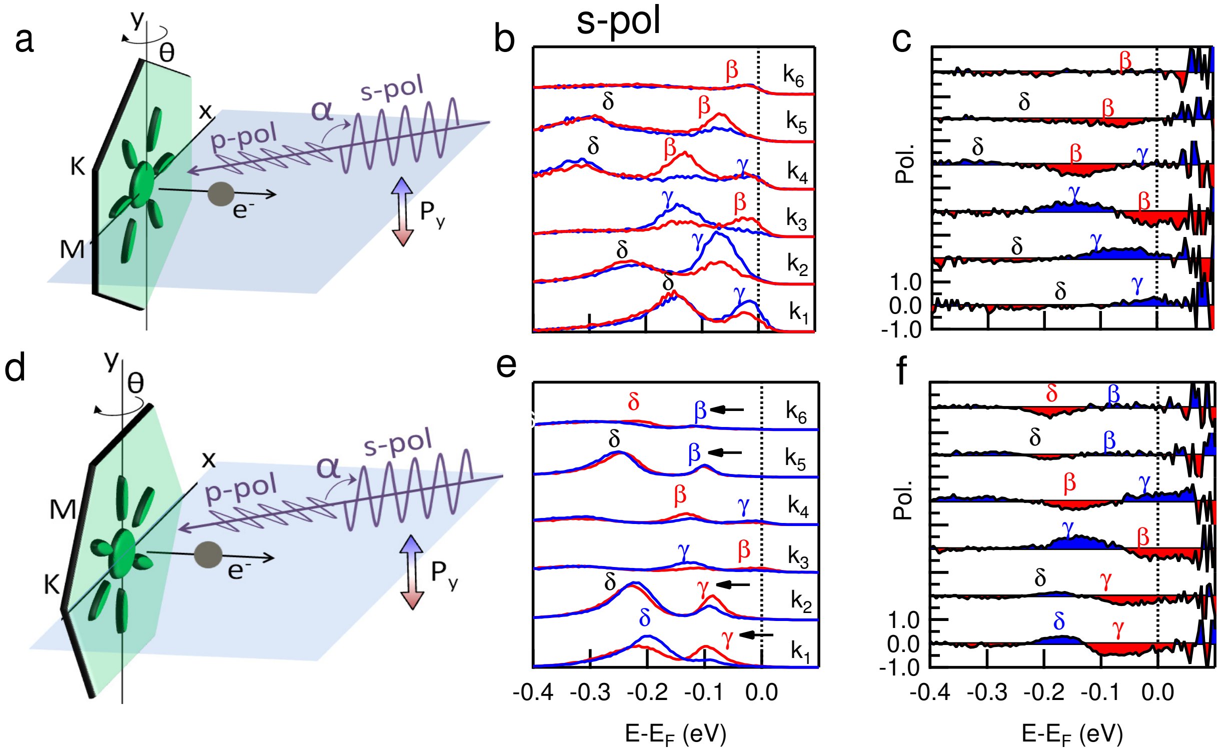

FIG. 3. **Spin-Resolved measurements with s-polarized light. a,** Experimental geometry for measurement along $\bar{\Gamma}$-$\bar{\mathrm{M}}$. The angle α of photon polarization can be rotated from p-polarized to s-polarized. **b,** Spin-resolved EDCs at momenta marked in a. Peaks are marked corresponding to bands in a. **c,** Spin-polarization corresponding to EDCs in b. **d-f** Same as a-c but along the $\bar{\Gamma}$-$\bar{\mathrm{K}}$ direction. In e, arrows mark the peaks that are not reversed relative to Fig. 2 with p-polarized light.

on photon polarization is seen near $\bar{\Gamma}$. P-polarized light, selecting p_x and p_z orbitals, shows the electron pocket enclosing $\bar{\Gamma}$ having $+P_y$ at $-k_x$ and $-P_y$ at $+k_x$. S-polarized light reveals the opposite spin polarizations for p_y orbitals near $\bar{\Gamma}$.

However, near $k_x \approx \pm 0.08\text{Å}^{-1}$, this behavior ceases, and for larger $|k|$, s-polarized light yields the same spin polarization as p-polarized in the lower surface band. This abrupt end to p_y having opposite spin of p_x and p_z orbitals is highlighted in Fig. 4f, showing rapid

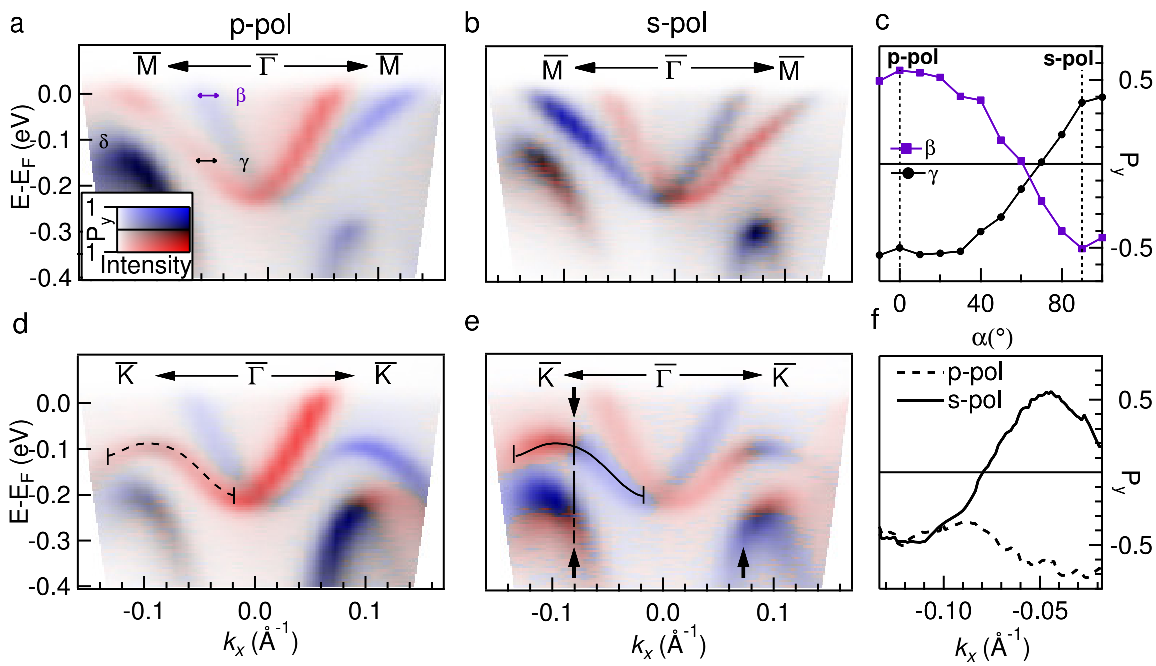

FIG. 4. **Spin-resolved maps of $\bar{\Gamma}$-$\bar{\mathrm{M}}$ and $\bar{\Gamma}$-$\bar{\mathrm{K}}$ direction of Sb(111). a,b** Spin-resolved maps of the $\bar{\Gamma}$-$\bar{\mathrm{M}}$ direction, taken with p-polarized (a) and s-polarized (b) light. The two-dimensional colorscale displays the total photoelectron intensity by relative darkness and the spin polarization by the balance of red and blue. **c,** Spin polarization of the two surface bands as a function of photon polarization angle. The bands are labeled in a, and spin polarizations were extracted at a fixed **k**, as indicated by the small regions marked with arrows. **d,e** Similar to a,b but with sample azimuth rotated to cut along $\bar{\Gamma}$-$\bar{\mathrm{K}}$. **f,** Spin polarization along the left branch of the lower band, as measured with both p- and s-polarized light. The stretch of **k** space plotted here is indicated by dispersive lines in d,e.

.

reversal of the spin polarization measured with s-polarized light in a fairly small range of **k** along the left half of the band dispersion. Along the same dispersion, p-polarized light yielded a constantly negative spin polarization. At high **k**, all orbitals in this band show $-P_y$

at $-k_x$ and $+P_y$ at $+k_x$ regardless of the photon polarization used. Such a transition cannot be captured by previously used two-band models[5,9], but is consistent with predictions made about photoemission from Bi_2Se_3[28] and the photon polarization-independent spin textures measured in its lower Dirac cone[8].

Besides the rapid change in spin texture of the lower surface band, an unusual spin polarization appears around the top of the bulk continuum to the left of the dashed line and arrows in Fig. 4g. In particular, the part of the valence band closest in energy to the surface band shows the opposite spin of the surface band: $+P_y$ at $-k_x$ and $-P_y$ at $+k_x$. Normally in the bulk limit of an inversion-symmetric, non-magnetic crystal, each state is spin-degenerate. Thus, these results are indicative of surface effects creating new surface states in addition to the topological surface states[23].

It is seen for the first time that the locking of orbital textures to distinct spin textures can be strongly momentum-dependent. It can change rapidly as the surface band mixes with other nearby bands, yielding similarly oriented spins for all p orbitals. On the other hand, symmetry requires the spin and orbital degrees of freedom to remain tied to each other along the mirror plane in $\mathbf{k}$ space.

IV. *AB INITIO* TIGHT-BINDING CALCULATIONS

To understand these findings, we performed an *ab initio* tight-binding simulation[7]. The basis is chosen to be the Sb p orbitals, and the hopping parameters and on-site energies for the surface and bulk regions were extracted from first-principles calculations within density functional theory (DFT) using the Quantum Espresso package[29]. Norm-conserving pseudopotentials with the local density approximation by Perdew-Zunger[30] were used for Sb in both scalar- and fully-relativistic forms. DFT calculations for periodic bulk and a

12-bilayer slab were performed to obtain the hopping parameters within the atomic orbital basis by Wannier90 code[31]. The 12-bilayer slab and the bulk DFT calculations are performed to extract the parameters for surface and bulk, respectively. In the tight-binding model, we separate the slab into top and bottom halves, and repeat the bulk unit cell in between to fill the two halves. The onsite energies in the bulk region are adjusted to match the middle layers in the 12-bilayer slab. Eventually a 90-bilayer slab is constructed. All the physical quantities such as band structures, spin textures, orbital projections and photoemission predictions are calculated from this tight-binding model following the method in Ref.[7]. In the tight-binding model, the SOC strength can be tuned by weighting the hopping parameters between those extracted from scalar- and fully-relativistic DFT calculations.

Fig. 5 shows the calculated p orbital-dependent spin textures and the simulated spin-ARPES results. The simulated spin measurements utilize the optical selection rule for the dominant p to s transitions, namely, that photons linearly polarized along the i-direction ($i = x, y, z$) will only allow a p_i to s transition (if spin-orbit effects in the light-matter interaction are neglected). Although the final states reached in the photoemission process can shape the measured spin polarization[32], the s-wave final states reached in this 6 eV experiment should accept any spin, yielding information about the initial state being probed. Our simulations included p_y orbitals, as probed by s-polarized light, and p_x orbitals, as probed by the x-component of p-polarized light. While p_z orbitals also contributed to the measurements with p-polarized light, their spins match those of p_x orbitals along the directions measured, allowing us to focus on a comparison of p_x and p_y only.

In Fig. 5, it is clear that in the vicinity of $\bar{\Gamma}$, the spin textures of the lower surface band are the same as those predicted for the Dirac cone in Bi_2Se_3[5,7,9], with p_y orbitals having opposite spin of p_x. However, when moving far enough away from $\bar{\Gamma}$ along the $\bar{\Gamma}$-$\bar{K}$ direction, the spin

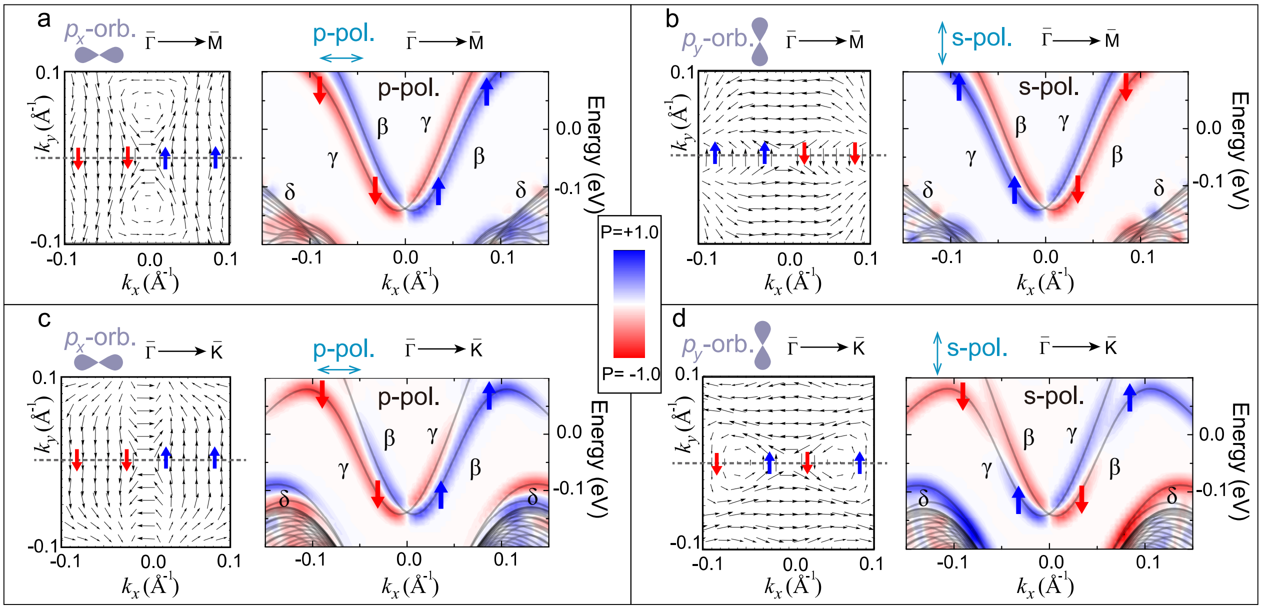

FIG. 5. **Calculated spin-orbital textures and simulated spin-ARPES plots. a,** Left panel: spin texture of p_x orbitals in the lower surface band, with $\hat{x}$ (horizontal dashed line) oriented along $\bar{\Gamma}$-$\bar{\mathrm{M}}$. These states can be photoemitted by p-polarized light. The black vectors are in-plane expectation values $\langle S_{x,y} \rangle$. Right panel: simulated spin-ARPES measurement along $\bar{\Gamma}$-$\bar{\mathrm{M}}$ using p-polarized light. Spin polarization of the p_x component of the bands is shown by the color from blue to red, while the band energies are indicated by gray lines. The spin polarization of the lower band (with arrows) is associated with the spin texture in the left panel. **b,** Left panel: spin texture of p_y orbitals in the lower surface band, with $\hat{x}$ oriented along $\bar{\Gamma}$-$\bar{\mathrm{M}}$. These states can be photoemitted by s-polarized light. Right panel: simulated spin-ARPES measurement along $\bar{\Gamma}$-$\bar{\mathrm{M}}$ using s-polarized light. **c,d,** Same as a,b, but now with $\hat{x}$ oriented along $\bar{\Gamma}$-$\bar{\mathrm{K}}$ and therefore the simulated measurements along $\bar{\Gamma}$-$\bar{\mathrm{K}}$. Note that in the lower band, the orbital dependence of the spin texture ceases at large $|k|$ for $\bar{\Gamma}$-$\bar{\mathrm{K}}$ but remains in $\bar{\Gamma}$-$\bar{\mathrm{M}}$, consistent with experimental results.

polarization of p_y orbitals matches that of p_x. We note that the calculations of the upper surface band reveal a similar end to the p orbital dependence of the spin orientation, albeit once the band is above the Fermi level in measurements. In contrast, the spin of p_y orbitals along $\bar{\Gamma}$-$\bar{\mathrm{M}}$ remains fixed opposite to p_x orbitals for all k.

The simulation of Fig. 5c,d shows another important aspect of the experiment: the apparent spin polarization around the top of the valence band as the surface state dispersion bends down towards it. From $\bar{\Gamma}$ to $\bar{\mathrm{K}}$, as is evident by the spin polarization, around $|k| = 0.06\mathring{A}^{-1}$ the lower surface band is decoupling from the upper surface band, and starts to pair with another surface state band that is closer in energy to the bulk valence continuum. Therefore, the experimentally observed spin polarization around the valence band top and below the topological surface bands should be attributed to this newly emerged surface band.

The results from Sb(111) indicate that the p orbital dependence of the spin texture breaks down as band mixing alters the basis states for the surface state wavefunction. This is highlighted by tuning the strength of SOC, α, in the tight-binding Hamitonian with $H_\alpha = H_0 + \alpha \Delta H_{SOC}$, where $\Delta H_{SOC} = H - H_0$, and H is the Hamiltonian with full SOC, and H_0 without SOC but with scalar relativistic effects. In addition to shrinking the bandgap, reducing α reduces the splitting between coupled bands, affording a clearer picture of which states are paired, meaning that they would be degenerate at each $\mathbf{k}$ without SOC ($\alpha = 0$). Fig. 6 shows the band structure with varying values of α. Violet is used to highlight the paired surface states. As shown in Fig. 6b, along the $\bar{\Gamma}$-$\bar{\mathrm{K}}$ direction, the lower topological surface band clearly couples with the upper topological surface band around the zone center. However, farther from $\bar{\Gamma}$, the two switch partners: the upper one runs into the conduction band continuum, and the other couples with a new surface state band which emerges above

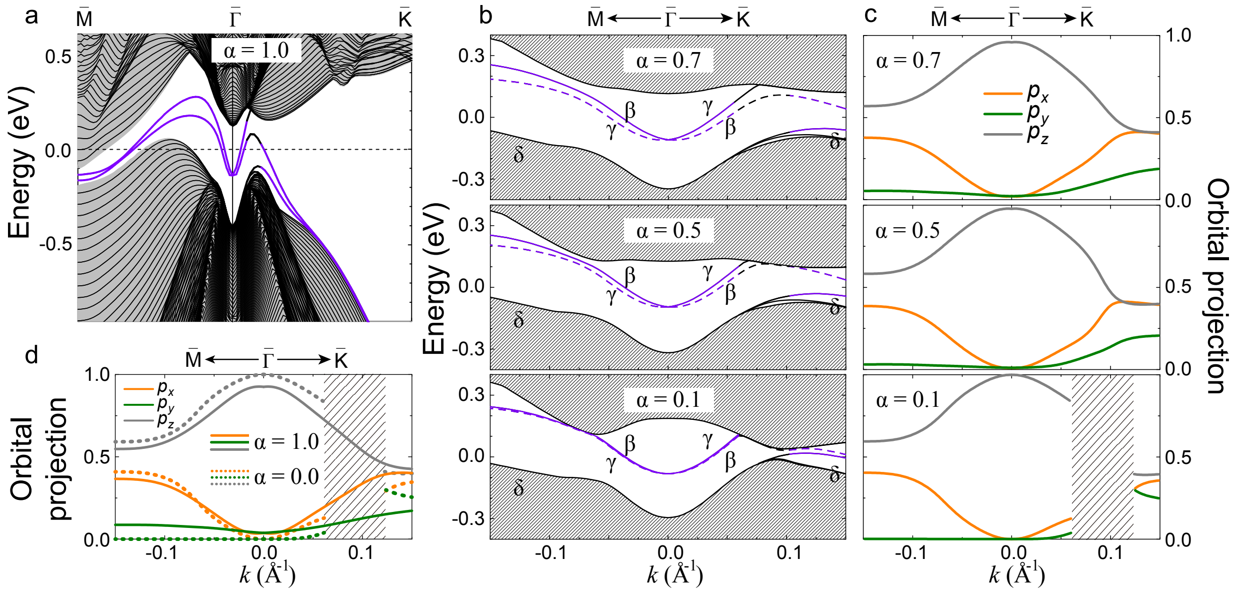

FIG. 6. **Band structure evolution with spin-orbit coupling strength (α). a,** Calculated 90-bilayer Sb band structures with full SOC ($\alpha = 1$). The darkly shaded area is the projection of bulk states onto the surface Brillouin zone. The violet color indicates the surface states that would be degenerate in the absence of SOC ($\alpha = 0$). **b,** Detailed band structures along two directions ($\bar{\mathrm{M}}$-$\bar{\Gamma}$-$\bar{\mathrm{K}}$), with different SOC strength α. Along $\bar{\Gamma}$-$\bar{\mathrm{M}}$, the two surface bands always couple to each other and stay within the gap; along $\bar{\Gamma}$-$\bar{\mathrm{K}}$, the lower surface band couples to the upper surface band near $k = 0$, then switches to a new surface band closer to the valence bulk continuum at larger $|k|$. **c,** Projected p orbital character at various SOC strengths along the lower topological surface band indicated by dashed lines in b. A rapid change in the orbital character is seen along the $\bar{\Gamma}$-$\bar{\mathrm{K}}$ direction. **d,** Similar to c, showing the two limits of full SOC ($\alpha = 1$, solid lines) and no SOC ($\alpha = 0$, dotted lines), respectively. Note that along $\bar{\Gamma}$-$\bar{\mathrm{K}}$, all orbitals have a finite projection even in the absence of SOC, whereas along $\bar{\Gamma}$-$\bar{\mathrm{M}}$, p_y is finite only with SOC. The missing parts of the curves in the $0.06 < k < 0.12$ range (shaded area) shown in c,d in the small α cases represent the fact that the band of interest disperses into the bulk continuum, as can be seen in b.

the bulk valence band. These two eventually disperse together into the bulk valence band continuum, as clearly shown in Fig. 6a with full spin-orbit effects considered. In contrast, along $\bar{\Gamma}$-$\bar{\mathrm{M}}$ (Fig. 6b), the two surface states of interest are always coupled to each other and remain within the gap, maintaining the p orbital dependence of their spins.

The surface bands appear in pairs at any individual $\mathbf{k}$ point due to the degeneracy when SOC is completely turned off. The presence of SOC will split the degenerate bands, highlighting the fact that each of the single surface bands connects the valence and conduction bulk continuum, a result of the topologically non-trivial nature of Sb.

In Sb, as in Bi_2Se_3, the electronic states around the Fermi level are dominated by $p_{x,y,z}$ orbitals, which can take on $S_z = \pm\frac{1}{2}$. In the topological surface states near $\bar{\Gamma}$, $\mathbf{L}$ and $\mathbf{S}$ are coupled in such a way that $J_z = \pm\frac{1}{2}$[5,9]. As shown in Fig. 6d, in the absence of SOC, at $\bar{\Gamma}$ there is only p_z character, i.e. the orbital projection is zero for p_x and p_y. An eigenstate of J_z will remain such even with $\mathbf{L}\cdot\mathbf{S}$ turned on. Thus, SOC will mix in $p_{x,y}$ orbitals, giving them a finite projection in 6c,d, while keeping $J_z = \pm\frac{1}{2}$ dominant in the vicinity of $\bar{\Gamma}$. This means that in this region, the states can be described sufficiently by a two-band model[5,9]. The $J_z = \pm\frac{1}{2}$ requirement determines the spin texture that each p orbital must have. In other words, for in-plane orbitals $|p_\pm\rangle = \frac{1}{\sqrt{2}}(\mp|p_x\rangle - i|p_y\rangle)$, with angular momentum $L_z = \pm 1$, the surface state can be constructed from two basis states, $|p_+, \downarrow\rangle$ and $|p_-, \uparrow\rangle$, carrying $J_z = \pm\frac{1}{2}$. Such states will always show a p orbital-dependent spin texture, meaning opposite spins will be measured with s-polarized and p-polarized light.

Symmetry provides similar constraints along $\bar{\Gamma}$-$\bar{\mathrm{M}}$. In the absence of SOC, mirror symmetry excludes p_y orbitals along this momentum direction because they cannot mix with $p_{x,z}$ orbitals. This is shown in Fig. 6d, where the $\alpha = 0$ case has a p_y projection of zero along the $\bar{\Gamma}$-$\bar{\mathrm{M}}$ line. Turning on SOC will mix in p_y orbitals (making their contribution finite along $\bar{\Gamma}$-$\bar{\mathrm{M}}$ in 6c,d) by allowing them to couple to spinors in a way that respects mirror symmetry, i.e. p_y will couple to the opposite spinor of that to which $p_{x,z}$ orbitals couple. The $p_{x,y}$ orbitals at $\bar{\Gamma}$, and the p_y orbitals along $\bar{\Gamma}$-$\bar{\mathrm{M}}$ are present only because of SOC and are subject to symmetry rules. Therefore, they are constrained in the spins to which they couple.

However, at high $|k|$ along $\bar{\Gamma}$-$\bar{\mathrm{K}}$, where there are not the same symmetry constraints, $p_{x,y}$ orbitals contribute appreciably even in the absence of SOC ($\alpha = 0$), as can be seen in 6d. Therefore, turning on SOC will change the orbital character only slightly here, and the properties detected with any photon polarization are primarily non-SOC effects. At high $|k|$, two basis states are no longer sufficient to describe the surface complexity, as is evident from the presence of extra bands along $\bar{\Gamma}$-$\bar{\mathrm{K}}$ in 6a. In this region with more states, more basis vectors are needed: $|p_+, \uparrow\rangle$ and $|p_-, \downarrow\rangle$, with $J_z = \pm\frac{3}{2}$. Generally, the inclusion of $J_z = \pm\frac{3}{2}$ components without symmetry constraints will alter the phase between the spin-up ($|\uparrow\rangle$) and spin-down ($|\downarrow\rangle$) components of the real spinor wavefunctions that couple to p orbitals, and may lead the spins not to reverse with different photon polarizations (e.g. non-zero linear combinations of $|p_+, \uparrow\rangle$ and $|p_+, \downarrow\rangle$ will never show this effect). This less constrained spin-orbital coupling along $\bar{\Gamma}$-$\bar{\mathrm{K}}$ is in contrast to $\bar{\Gamma}$ and $\bar{\Gamma}$-$\bar{\mathrm{M}}$, where symmetry protects the way that $J_z = \pm\frac{1}{2}$ and $J_z = \pm\frac{3}{2}$ mix, preserving the observation of opposite spins with different photon polarizations. Lastly, we note that hexagonal warping effects[33], could not be responsible for the sudden change of the spin texture at large $|k|$ because they do not alter the orbital texture and instead just diminish the magnitude of in-plane spin polarizations.

V. CONCLUSION

This work shows that the coupling between the spin textures and orbital textures can vary across the Brillouin zone. Knowledge of the full complexity of a surface state's wavefunction, including the symmetry rules governing the coupling of spin and orbital degrees of freedom, is a fundamental prerequisite for its application to spintronics or other technologies. One would expect to see orbitals with different spin orientations in the parts of a spin-orbit material's surface Brillouin zone where various symmetries protect it. Away from these momenta, surface states are allowed to mix with other states, ending the requirement that each orbital character couple to distinct spin textures. This picture provides an understanding of the full complexity of a surface state's spin degree of freedom.

ACKNOWLEDGMENTS

The experimental work was supported by the U.S. Department of Energy (DOE), Office of Science, Office of Basic Energy Sciences, Materials Sciences and Engineering Division, under Contract No. DE-AC02-05CH11231 within the Quantum Materials Program (KC2202). The theoretical work was supported by the U.S. Department of Energy (DOE), Office of Science, Office of Basic Energy Sciences, Materials Sciences and Engineering Division, under Contract No. DE-AC02-05CH11231 within the Theory of Materials Program (KC2301) which provided the DFT calculations; and by the National Science Foundation under Grant No. DMR-1508412 which provided the tight-binding calculations. Computational resources have been provided by the National Energy Research Scientific Computing Center (NERSC), a DOE Office of Science User Facility supported by the Office of Science of the U.S. Department of Energy under Contract No. DE-AC02-05CH11231 and the Extreme Science and Engineering Discovery Environment (XSEDE), which is supported by National Science Foundation Grant No. ACI-1053575. K.G. was supported by a fellowship from the National Science Foundation under Grant No. DGE 1106400. J.H.R. and C.- H.P. were supported by Creative-Pioneering Researcher Program through Seoul National University.

---

* These authors contributed equally to the preparation of this manuscript.

† sglouie@berkeley.edu

‡ alanzara@lbl.gov

[1] S. Datta and B. Das, Appl. Phys. Lett. **56**, 665 (1990).

[2] I. Zutić, J. Fabian, and S. Das Sarma, Rev. Mod. Phys. **76**, 323 (2004).

[3] D. D. Awschalom and M. E. Flatte, Nat Phys **3**, 153 (2007).

[4] J. E. Moore, Nature **464**, 194 (2010).

[5] H. Zhang, C.-X. Liu, and S.-C. Zhang, Phys. Rev. Lett. **111**, 066801 (2013).

[6] Y. Cao, J. A. Waugh, X.-W. Zhang, J.-W. Luo, Q. Wang, T. J. Reber, S. K. Mo, Z. Xu, A. Yang, J. Schneeloch, G. D. Gu, M. Brahlek, N. Bansal, S. Oh, A. Zunger, and D. S. Dessau, Nat Phys **9**, 499 (2013).

[7] Z.-H. Zhu, C. N. Veenstra, G. Levy, A. Ubaldini, P. Syers, N. P. Butch, J. Paglione, M. W. Haverkort, I. S. Elfimov, and A. Damascelli, Phys. Rev. Lett. **110**, 216401 (2013).

[8] Z. Xie, S. He, C. Chen, Y. Feng, H. Yi, A. Liang, L. Zhao, D. Mou, J. He, Y. Peng, X. Liu, Y. Liu, G. Liu, X. Dong, L. Yu, J. Zhang, S. Zhang, Z. Wang, F. Zhang, F. Yang, Q. Peng, X. Wang, C. Chen, Z. Xu, and X. J. Zhou, Nat Commun **5**, 3382 (2014).

[9] C.-H. Park and S. G. Louie, Phys. Rev. Lett. **109**, 097601 (2012).

[10] C. Jozwiak, C.-H. Park, K. Gotlieb, C. Hwang, D.-H. Lee, S. G. Louie, J. D. Denlinger, C. R. Rotundu, R. J. Birgeneau, Z. Hussain, and A. Lanzara, Nat Phys **9**, 293 (2013).

[11] Z.-H. Zhu, C. N. Veenstra, S. Zhdanovich, M. P. Schneider, T. Okuda, K. Miyamoto, S.-Y. Zhu, H. Namatame, M. Taniguchi, M. W. Haverkort, I. S. Elfimov, and A. Damascelli, Phys. Rev. Lett. **112**, 076802 (2014).

[12] H. Mirhosseini, J. Henk, A. Ernst, S. Ostanin, C.-T. Chiang, P. Yu, A. Winkelmann, and J. Kirschner, Phys. Rev. B **79**, 245428 (2009).

[13] C. N. Veenstra, Z.-H. Zhu, M. Raichle, B. M. Ludbrook, A. Nicolaou, B. Slomski, G. Landolt, S. Kittaka, Y. Maeno, J. H. Dil, I. S. Elfimov, M. W. Haverkort, and A. Damascelli, Phys. Rev. Lett. **112**, 127002 (2014).

[14] S. N. P. Wissing, A. B. Schmidt, H. Mirhosseini, J. Henk, C. R. Ast, and M. Donath, Phys. Rev. Lett. **113**, 116402 (2014).

[15] H. Mirhosseini, M. Flieger, and J. Henk, New Journal of Physics **15**, 033019 (2013).

[16] K. Miyamoto, H. Wortelen, H. Mirhosseini, T. Okuda, A. Kimura, H. Iwasawa, K. Shimada, J. Henk, and M. Donath, Phys. Rev. B **93**, 161403 (2016).

[17] H. Maaß, H. Bentmann, C. Seibel, C. Tusche, S. V. Eremeev, T. R. F. Peixoto, O. E. Tereshchenko, K. A. Kokh, E. V. Chulkov, J. Kirschner, and F. Reinert, Nat Commun **7**, (2016).

[18] K. Sugawara, T. Sato, S. Souma, T. Takahashi, M. Arai, and T. Sasaki, Phys. Rev. Lett. **96**, 046411 (2006).

[19] T. Kadono, K. Miyamoto, R. Nishimura, K. Kanomaru, S. Qiao, K. Shimada, H. Namatame, A. Kimura, and M. Taniguchi, Applied Physics Letters **93**, 252107 (2008).

[20] D. Hsieh, Y. Xia, L. Wray, D. Qian, A. Pal, J. H. Dil, J. Osterwalder, F. Meier, G. Bihlmayer, C. L. Kane, Y. S. Hor, R. J. Cava, and M. Z. Hasan, Science **323**, 919 (2009).

[21] G. Bian, T. Miller, and T.-C. Chiang, Phys. Rev. Lett. **107**, 036802 (2011).

[22] M. Bianchi, D. Guan, A. Stróżecka, C. H. Voetmann, S. Bao, J. I. Pascual, A. Eiguren, and P. Hofmann, Phys. Rev. B **85**, 155431 (2012).

[23] A. Takayama, T. Sato, S. Souma, and T. Takahashi, New Journal of Physics **16**, 055004 (2014).

[24] C. Jozwiak, J. Graf, G. Lebedev, N. Andresen, A. K. Schmid, A. V. Fedorov, F. El Gabaly, W. Wan, A. Lanzara, and Z. Hussain, Rev. Sci. Instrum. **81**, 053904 (2010).

[25] K. Gotlieb, Z. Hussain, A. Bostwick, A. Lanzara, and C. Jozwiak, Rev. Sci. Instrum. **84**, 093904 (2013).

[26] K. Kuroda, K. Yaji, M. Nakayama, A. Harasawa, Y. Ishida, S. Watanabe, C.-T. Chen, T. Kondo, F. Komori, and S. Shin, Phys. Rev. B **94**, 165162 (2016).

[27] H. Wortelen, H. Mirhosseini, K. Miyamoto, A. B. Schmidt, J. Henk, and M. Donath, Phys. Rev. B **91**, 115420 (2015).

[28] J. H. Ryoo and C.-H. Park, Phys. Rev. B **93**, 085419 (2016).

[29] P. Giannozzi, S. Baroni, N. Bonini, M. Calandra, R. Car, C. Cavazzoni, D. Ceresoli, G. L. Chiarotti, M. Cococcioni, I. Dabo, A. D. Corso, S. de Gironcoli, S. Fabris, G. Fratesi, R. Gebauer, U. Gerstmann, C. Gougoussis, A. Kokalj, M. Lazzeri, L. Martin-Samos, N. Marzari, F. Mauri, R. Mazzarello, S. Paolini, A. Pasquarello, L. Paulatto, C. Sbraccia, S. Scandolo, G. Sclauzero, A. P. Seitsonen, A. Smogunov, P. Umari, and R. M. Wentzcovitch, Journal of Physics: Condensed Matter **21**, 395502 (2009).

[30] J. P. Perdew and A. Zunger, Phys. Rev. B **23**, 5048 (1981).

[31] A. A. Mostofi, J. R. Yates, Y.-S. Lee, I. Souza, D. Vanderbilt, and N. Marzari, Computer Physics Communications **178**, 685 (2008).

[32] J. Sánchez-Barriga, A. Varykhalov, J. Braun, S.-Y. Xu, N. Alidoust, O. Kornilov, J. Minár, K. Hummer, G. Springholz, G. Bauer, R. Schumann, L. V. Yashina, H. Ebert, M. Z. Hasan, and O. Rader, Phys. Rev. X **4**, 011046 (2014).

[33] L. Fu, Phys. Rev. Lett. **103**, 266801 (2009).